Special Issue
Toward Suppression of Hydrogen Absorption and Hydrogen Embrittlement for Steels

ISIJ International, Vol. 61 (2021), No. 4, pp. 1278–1286
https://doi.org/10.2355/isijinternational.ISIJINT-2019-510

Hydrogen-assisted Crack Propagation in Pre-strained Twinning-induced Plasticity Steel: from Initiation at a Small Defect to Failure

Abbas MOHAMMADI,[1)] Motomichi KOYAMA,[2)]* Gregory GERSTEIN,[3)] Hans Jürgen MAIER[3)] and Hiroshi NOGUCHI[1)]

1) Faculty of Engineering, Kyushu University, 744 Motooka, Nishiku, Fukuoka, 819-0395 Japan.
2) Institute for Materials Research, Tohoku University, 2-1-1 Katahira, Aoba-ku, Sendai, 980-8577 Japan.
3) Institut für Werkstoffkunde (Materials Science), Leibniz Universität Hannover, An der Universität 2, Garbsen, 30823 Germany.

(*Received on August 12, 2019; accepted on December 12, 2019; J-STAGE Advance published date: May 25, 2020*)

Hydrogen-assisted crack growth of pre-strained twinning-induced plasticity (TWIP) steel was investigated using artificial defects (micro-drilled holes), which acted as artificial crack initiation sites. Hydrogen was introduced into the specimens by electrochemical hydrogen charging during slow strain rate tensile test. The quasi-cleavage crack propagation observed was due to repeated crack initiation near the crack tip and subsequent coalescence. Crack initiation near the crack tip occurred after plastic deformation of the crack tip, and pre-straining facilitated plasticity-driven crack initiation. The early stage of plasticity-driven crack growth was sensitive to the crack length and remote stress level. Accordingly, the crack growth rate in the early stage increased with the increase in the initial defect size. In the following stage of the crack growth, the crack growth rate exhibited a complicated trend with respect to the crack length, which is possibly due to the plastic-wake-altered stress field around the crack tip, which depends on the initial defect size.

KEY WORDS: hydrogen embrittlement; twinning-induced plasticity steel; crack propagation; quasi-cleavage; pre-strain.

1. Introduction

A well-known property of stable austenitic steels is their superior hydrogen embrittlement resistance.[1–3)] Even when hydrogen-induced mechanical degradation appears, failure occurs after significant plastic deformation.[4,5)] More specifically, even if crack initiation occurs at an early deformation stage, most of the cracks blunt and stop growing once, *i.e.*, the microstructural damage, is arrested.[6–8)] Therefore, the risk of hydrogen-induced fracture in solution-treated austenitic steels is rather small as compared to martensitic steels.

Nevertheless, hydrogen embrittlement in austenitic steels is recognized as an important problem, which is probably due to pre-strain effects. The effect of plastic pre-strains is an important factor in failure of austenitic steels even without hydrogen.[9,10)] In particular, the formation and growth of cracks and voids can result from the accumulation of lattice defects, such as vacancies,[11,12)] dislocations,[13,14)] and twins,[15,16)] which reduces the stress accommodation capability and creates a microstructural crack growth path. In addition, plasticity-induced damage can act together with hydrogen effects.[17)] Especially at room temperature, plasticity-induced damage will occur during forming processes of structural components such as automobile parts. Thus, it is practically important to note that a certain number of plastically deformed austenitic steel components may exhibit a potential risk for failure associated with the deterioration of small crack arrestability. Furthermore, cold/warm pre-deformation is often used for austenitic steel to increase the yield strength, which is another route that introduces plasticity-induced damage. To better understand the hydrogen embrittlement resistance of high strength and ductile materials, such as austenitic steels and the variants derived from these, the effect of plastic pre-deformation on hydrogen-assisted crack propagation needs to be considered.

High-Mn twinning-induced plasticity (TWIP) steels are typical examples of austenitic steels with high strength; however, they also exhibit hydrogen embrittlement after

* Corresponding author: E-mail: koyama@imr.tohoku.ac.jp

significant plastic deformation.[18,19] Moreover, these types of steels show hydrogen-induced delayed failure when the structural components are severely plastically deformed.[20,21] In the present study, hydrogen-assisted crack propagation behavior of a plastically pre-deformed TWIP steel was investigated with a focus on crack propagation rate and the associated microstructural evolution. To shed light on the influence of micro defects under hydrogen charging conditions, artificial defects with different sizes were introduced into the samples.

2. Experimental Procedures

As an example of structural materials for automobile parts, we received a warm-rolled Fe-15Mn-2.5Si-2.5Al-0.7C (wt.%) fully austenitic TWIP steel.[22] The warm rolling was performed to increase strength level. In this study, we evaluate a pre-strain effect on crack propagation in the practically designed steel. **Figure 1**(a) shows the microstructure in the as-received condition in the form of a rolling direction inverse pole figure (RD-IPF) map, which demonstrates the presence of almost bimodal grain size distribution. In fact, as can be seen in Fig. 1(b), the grain size can be classified into two groups: fine grains below 20 μm (indicated by the area fraction and number fraction curves shown in Fig. 1(b)) and coarse grains of approximately 100 μm (indicated by the area fraction curve shown in Fig. 1(b)). The mean grain size, including coarse and fine grains and twin boundaries, is $\approx$ 25 μm.

Tensile specimens, with gauge dimensions of 4 mm in width, 0.3 mm in thickness, and 10 mm in length, were cut by electrical discharge machining (EDM). Following EDM, the thickness of the specimens was reduced by mechanical grinding to remove any EDM-induced surface artefacts.

To investigate the effect of plastic pre-deformation on crack propagation behavior, the specimens were first pre-deformed in tension up to a 30% strain at an initial strain rate of 10^{-5} s^{-1}. Thereafter, the surface of the specimens was mechanically polished to a mirror finish grade. Next, two types of artificial small stress concentration sources were introduced by micro-drilling technique in the central section of the gauge part. In part of the specimens, one micro-drill hole (1DH) with a diameter of 300 μm was introduced. The subsequent tests for them were conducted in both the hydrogen-charged and uncharged conditions. In addition, three drill holes (3DH) with diameters of 300 μm, which were placed next to each other on the centerline perpendicular to the tensile direction, were machined in another set of samples. The final configuration of the specimens is given in **Fig. 2**.

Tensile tests with the pre-strained samples with the micro-drill holes were conducted with and without hydrogen charging at a crosshead speed of 10^{-4} mm/s at temperature of 295 K. Crack propagation was observed by in-situ using an optical microscope with a focal length of 10 cm. Optical images were taken every 30 s until the end of the test. For part of the samples, hydrogen was introduced during the tensile test by electrochemical charging in a 3% NaCl aqueous solution containing 3 g/L NH_4SCN at a current density of 30 A/m^2. A platinum wire was employed as the counter electrode.

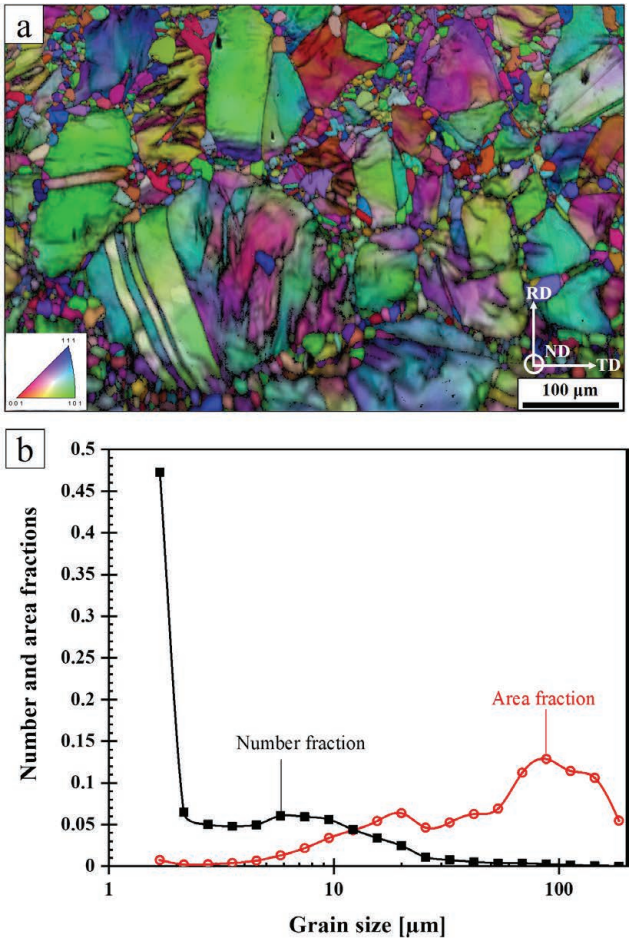

Fig. 1. (a) Rolling direction inverse pole figure (RD-IPF) map superimposed by image quality (IQ) contrast and (b) histograms demonstrating the bimodal grain size distribution of the initial microstructure. (Online version in color.)

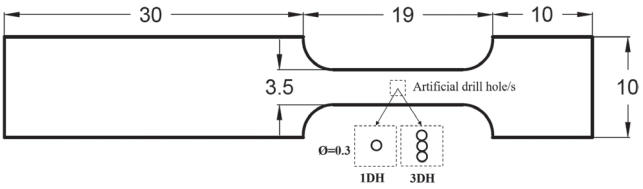

Fig. 2. Tensile specimen geometry with illustration of the two sets of artificial defects introduced (all dimensions are in mm); the specimen thickness is 0.25 mm.

The fracture surfaces were observed by scanning electron microscopy (SEM) at an accelerating voltage of 15 kV. In addition, the SEM was used for secondary electron imaging and electron backscatter diffraction (EBSD) measurements to correlate cracks with the microstructure near the fracture surfaces of the hydrogen-charged specimens. For the microstructure observations, the specimens were mechanically polished using colloidal silica with a particle size of 60 nm. All EBSD measurements were performed at an acceleration voltage of 20 kV with a beam step size of 100 nm.

3. Results

3.1. Hydrogen Effects on Mechanical Response

Figure 3 shows the engineering stress–displacement diagrams for the 30% pre-strained specimens. The engineering

stress was evaluated as

$$\sigma_e = \frac{P}{A_0}, \quad \text{..... (1)}$$

where P and A_0 are the applied load and initial net cross-sectional area, respectively. The uncharged 1DH specimen exhibited failure at a displacement of 0.47 mm (indicated by the dashed line in Fig. 3). Hydrogen charging resulted in a loss of ≈ 15% of the overall displacement (1DH: black solid line in Fig. 3). Accordingly, the ultimate tensile strength (UTS) also decreased from 1 135 MPa to 1 015 MPa due to the hydrogen charging. Furthermore, an increase in drill hole number (3DH specimen) showed an additional reduction in ductility compared with the case of the hydrogen-charged 1DH specimen (red line in Fig. 3).

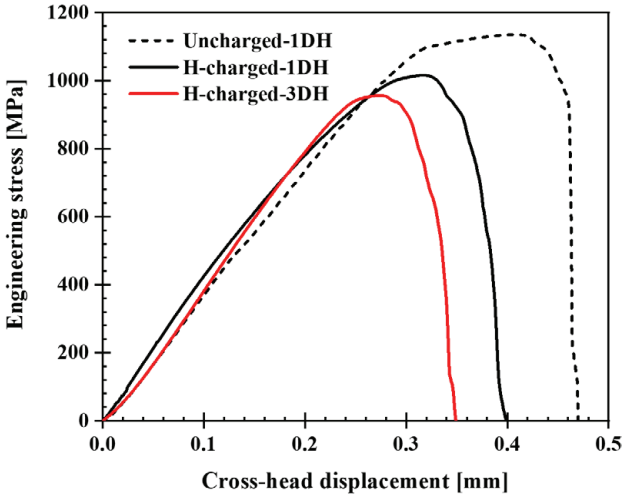

Fig. 3. Engineering stress–displacement curves demonstrating the effect of hydrogen charging on mechanical behavior upon straining in tension. (Online version in color.)

3.2. Crack Propagation Behavior in the Hydrogen-charged Specimen

Figure 4 shows optical images taken by in-situ optical microscopy during tensile testing in the hydrogen-charged 1DH specimen. Following evolution of the plastic zone near the drill hole, cracks initiated from both sides of the micro-hole, as shown in Fig. 4(b), and gradually grew perpendicular to the tensile axis until fracture as shown in Figs. 4(c)–4(f). In **Fig. 5**, the crack length measured from the in-situ images is plotted as a function of time and engineering stress. Here, the crack length is defined as the projected crack length including the size of initial drill hole. The crack propagation can be divided into two stages of low and high

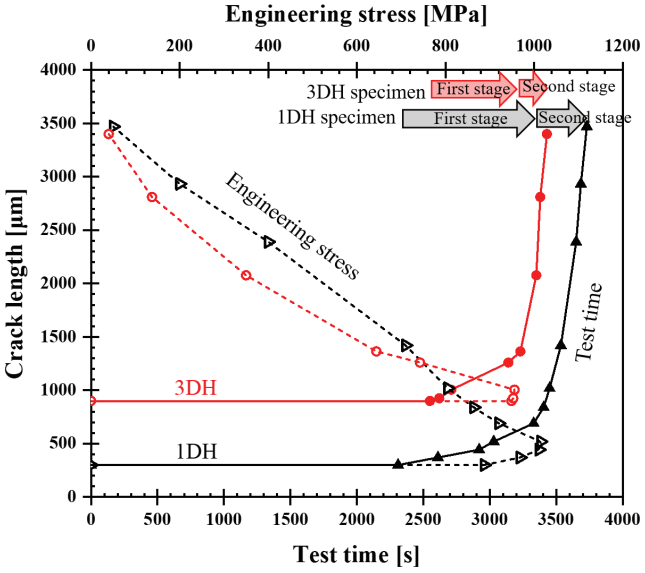

Fig. 5. Crack length as a function of test time (solid line) and engineering net sectional stress (dashed line) for the hydrogen-charged specimens; the black and red lines represent 1DH and 3DH specimens, respectively. (Online version in color.)

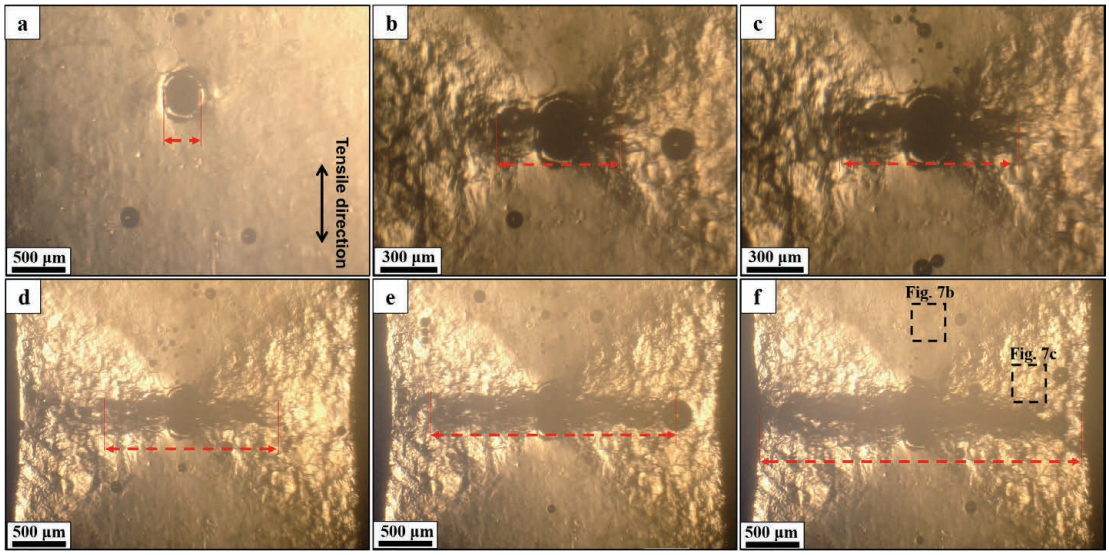

Fig. 4. Optical images of crack propagation in the hydrogen-charged 1DH specimen taken in-situ: (a) before the tensile test (note drill hole with a diameter of 300 μm), (b) crack length of 520 μm at 3 000 s and a displacement of 0.3 mm, (c) crack length of 850 μm at 3 400 s and a displacement of 0.34 mm, (d) crack length of 1 420 μm at 3 550 s and a displacement of 0.355 mm, (e) crack length of 2 400 μm at 3 650 s and a displacement of 0.365 mm, and (f) facture point at a displacement of 0.4 mm. (Online version in color.)

crack propagation rate. The first stage is defined from the point of initiation up to the critical point where rapid propagation is triggered. The following stage up to final failure is defined as the second stage. Following crack initiation, the rate of crack propagation sharply increased until failure in the two stages (solid lines in Fig. 5). However, with respect to net engineering stress (dashed lines), it progressed in a more gradual way, which indicates that the fracture mode was not completely brittle.

Figure 6 shows the true net sectional stress as a function of the total crack length for the hydrogen-charged specimens. The true net sectional stress was defined as

$$\sigma_T = \frac{P}{A_f}, \quad \text{..... (2)}$$

where P and A_f are the applied load and local cross-sectional area, respectively. In Fig. 6, the black and red lines indicate the results of 1DH and 3DH specimens, respectively. As can be seen, the stress gradually reduces after the maximum for the 3DH specimen, whereas it becomes nearly constant due to the increase in the crack length in the 1DH specimen. These results demonstrate that the apparent stress level in the 1DH specimen is higher than that in the 3DH specimen when compared at the same crack length. The difference in the stress levels of the 1DH and 3DH specimens increases after the maximum value of the 3DH specimen, which cor-

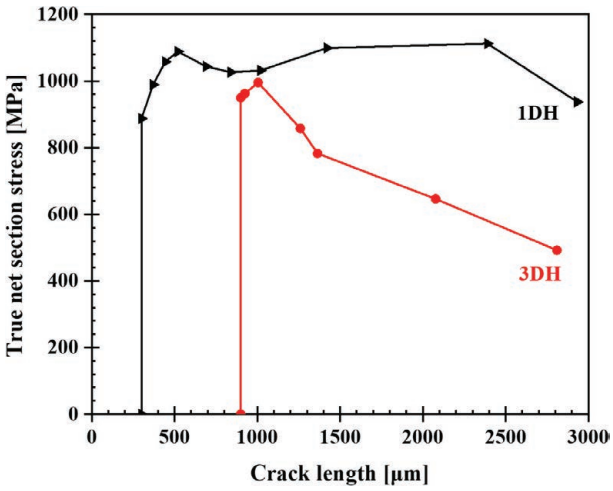

Fig. 6. True net sectional stress as a function of the total crack length in hydrogen-charged specimens. (Online version in color.)

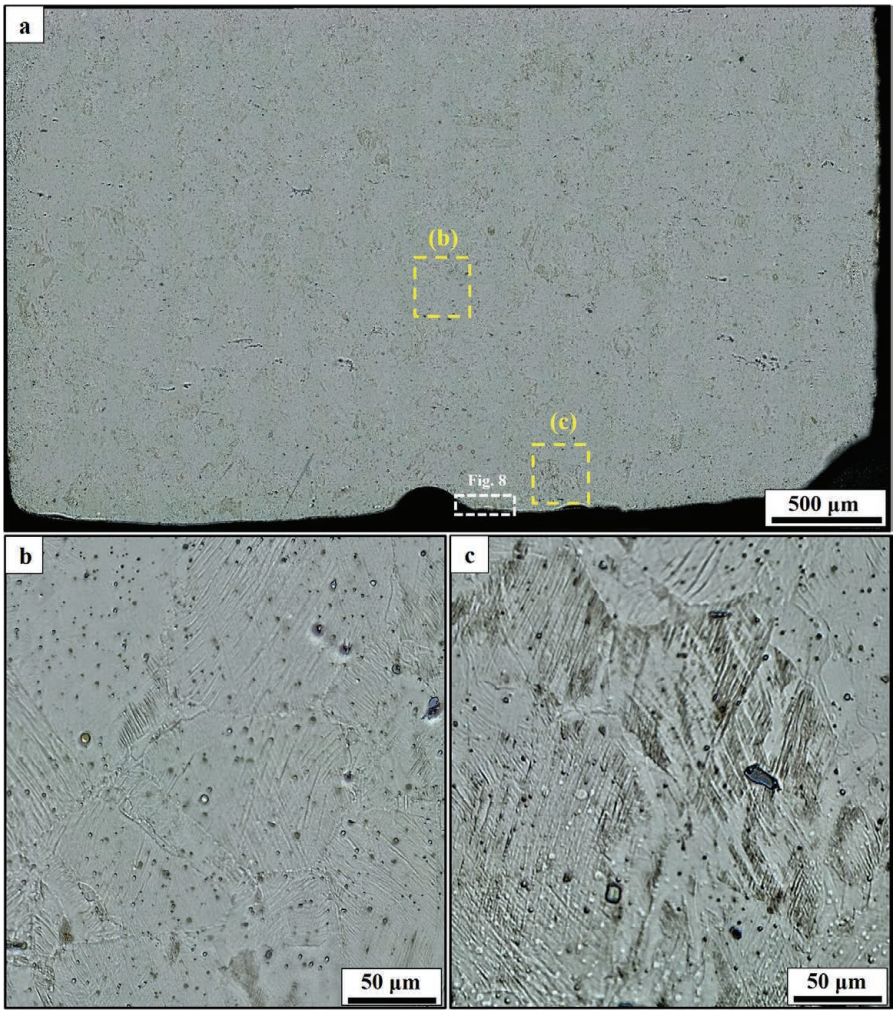

Fig. 7. Overview and higher magnification details demonstrating the difference in microstructural evolution in the hydrogen-charged 1DH specimen after failure: (a) yellow boxes marked areas with (b) low density of twining further away from the micro-hole along the tensile direction and (c) high density of twins in the vicinity of the fracture surface. The positions shown in panels (b) and (c) correspond to the locations indicated in Fig. 4(f). (Online version in color.)

responds to the second stage shown in Fig. 5.

Figure 7(a) shows the overall microstructure distribution of the hydrogen-charged 1DH specimen after failure. Owing to the presence of the micro-hole (stress concentration source), a heterogeneous distribution of the deformation microstructures, such as twins were observed, c.f. Figs. 7(b) and 7(c). Specifically, the twin density at the region further away from the micro-hole along the tensile direction is lower than that in the vicinity of the fracture surface. It should be noted that there were only a few micro cracks on the specimen surface after fracture, which is different from that in the case of a tested smooth TWIP steel plate, where numerous secondary cracks were observed after fracture due to hydrogen charging.[22)]

Figure 8 shows an SEM image and the corresponding RD-IPF map near the fracture surface of the 1DH specimen. As can be seen in Fig. 8(a), a secondary crack initiated from the micro-hole. In addition, the RD-IPF map in Fig. 8(b) shows that the small secondary crack that had formed from

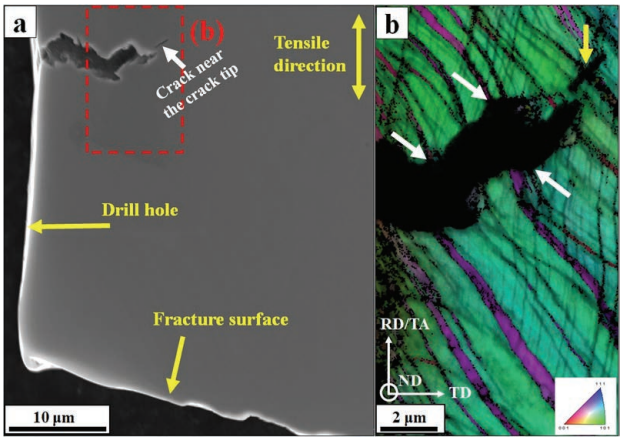

Fig. 10. (a) SEM image showing a crack ahead of a secondary crack tip near the fracture surface for a hydrogen-charged 3DH specimen. (b) RD-IPF map in the location outlined by the red dashed line in (a). The RD-IPF map is superimposed on the IQ map. (Online version in color.)

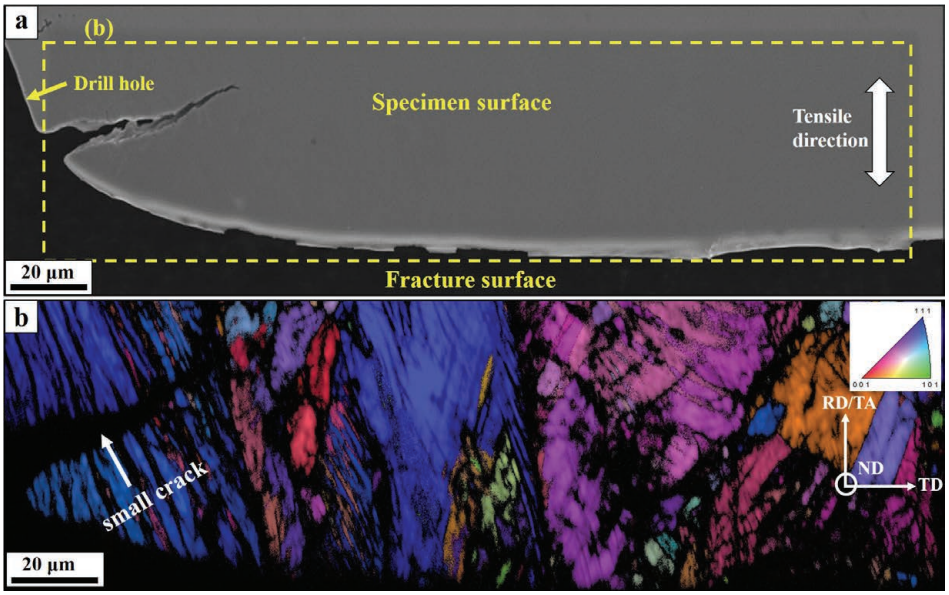

Fig. 8. (a) SEM image and (b) corresponding RD-IPF map of the surface at one side of the micro-hole in the vicinity of the fracture surface of the hydrogen-charged 1DH specimen after the tensile test; the RD-IPF map has been superimposed with IQ contrast. (Online version in color.)

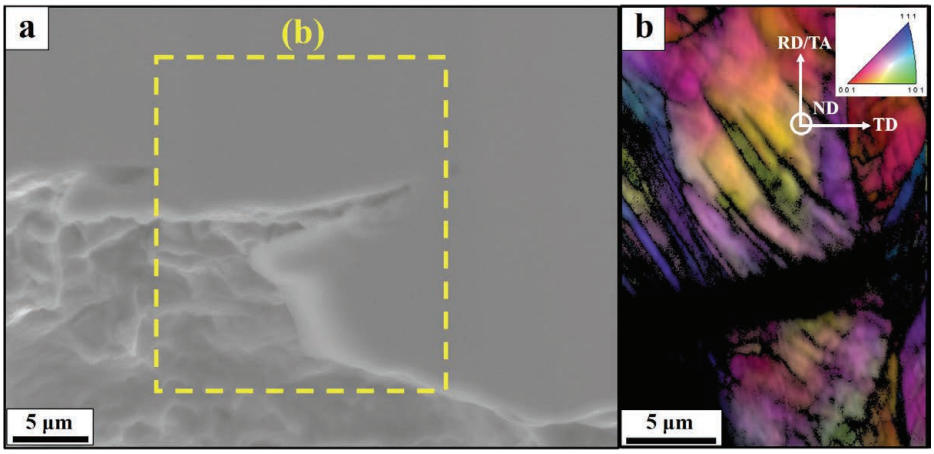

Fig. 9. (a) SEM image and (b) corresponding RD-IPF map of the surface crack in the vicinity of the fracture surface in a hydrogen-charged 3DH specimen; the RD-IPF map has been superimposed with IQ contrast. (Online version in color.)

the micro-hole propagated in the grain interior, and finally terminated at the grain boundary. Furthermore, the plate-like microstructure with a different orientation from the matrix and low image quality index shown in Fig. 8(b) indicates the formation of deformation twins within the grain interior. The hydrogen-charged 3DH specimen shown in **Fig. 9** also exhibited transgranular crack propagation and formation of deformation twins.

Figure 10(a) shows another example of an SEM image near the fracture surface of the hydrogen-charged 3DH specimen. This image demonstrates the crack initiation in front of the secondary crack tip. The corresponding RD-IPF map taken near the secondary crack tip (Fig. 10(b)) shows a considerable number of deformation twin plates. Specifically, both the secondary crack and associated small crack propagated across the deformation twin plates. **Figure 11** shows a set of SEM and EBSD images taken around the fracture surface in the 1DH and 3DH specimens. The RD-IPF maps shown in Figs. 11(a_2) and 11(b_2) show a considerable amount of lattice distortion associated with plastic deformation including the effect of deformation twins.[23,24] However, the lattice distortion distribution, which can mainly be attributed to the presence of geometrically necessary dislocations, did not show a significant difference between the hydrogen-charged 1DH and 3DH specimens, as demonstrated by the kernel average misorientation (KAM)[25–27] and grain reference orientation deviation (GROD) maps[28,29] (Figs. 11(a_3) and 11(b_3) and Figs. 11(a_4) and 11(b_4,) respectively). This is possibly due to the effect of the large plastic pre-strain.

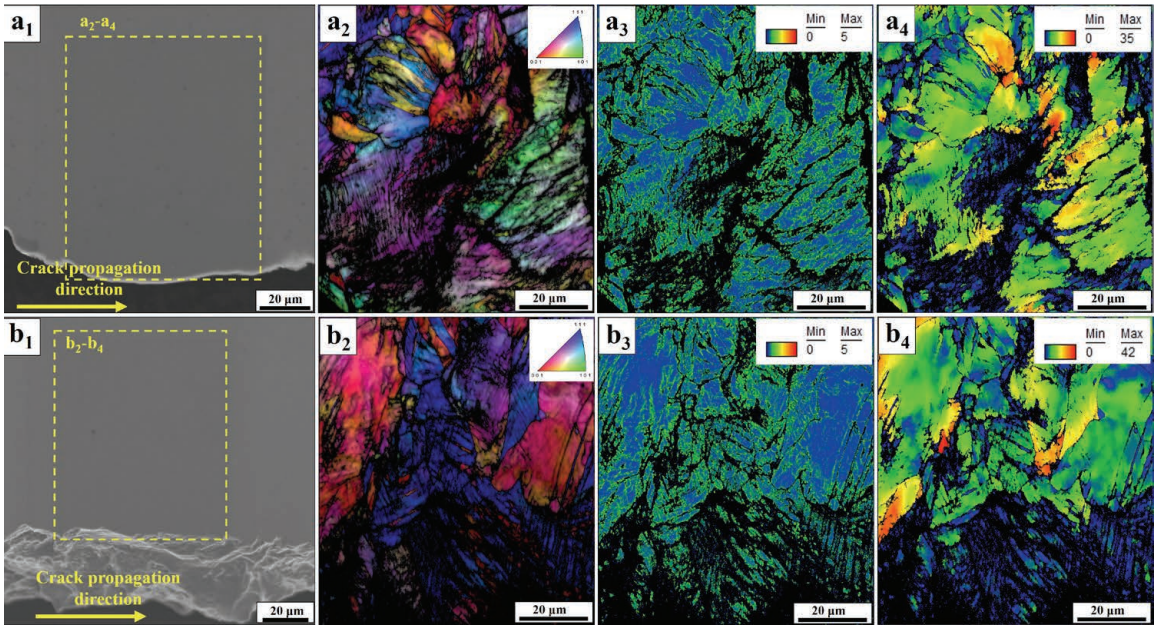

Fig. 11. SEM images and corresponding EBSD results obtained for the hydrogen-charged (a) 1DH and (b) 3DH specimens at an identical distance of 700 μm from the center of the micro-drill hole; indices 1, 2, 3, and 4 indicate the SEM image, RD-IPF map, kernel average misorientation (KAM) map, and grain reference orientation deviation (GROD) map, respectively. (Online version in color.)

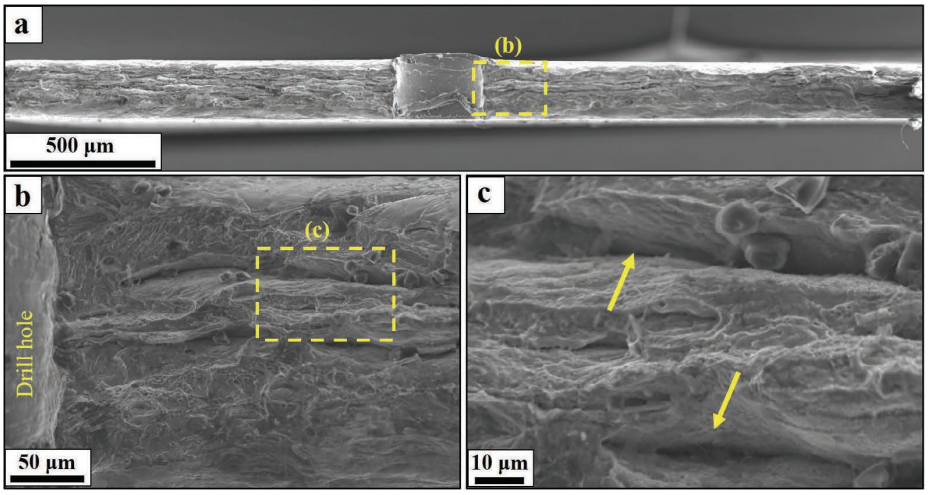

Fig. 12. (a) Overview SEM image of the fracture surface of the uncharged 1DH specimen. High-magnification details of the area highlighted in (a) are shown in (b) and (c) where arrows mark delamination events. (Online version in color.)

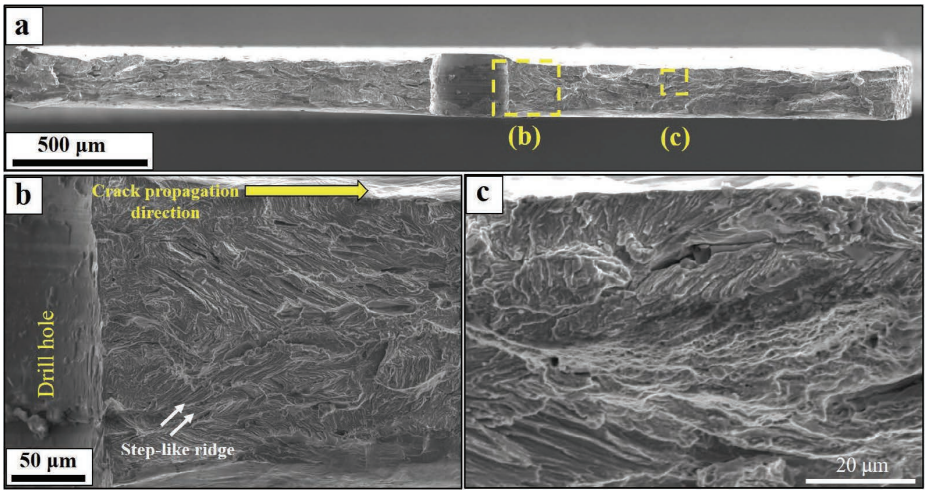

Fig. 13. (a) Overview SEM image of the fracture surface of the hydrogen-charged 1DH specimen. High-magnification details of the areas highlighted in (a) are shown in (b) and (c). (Online version in color.)

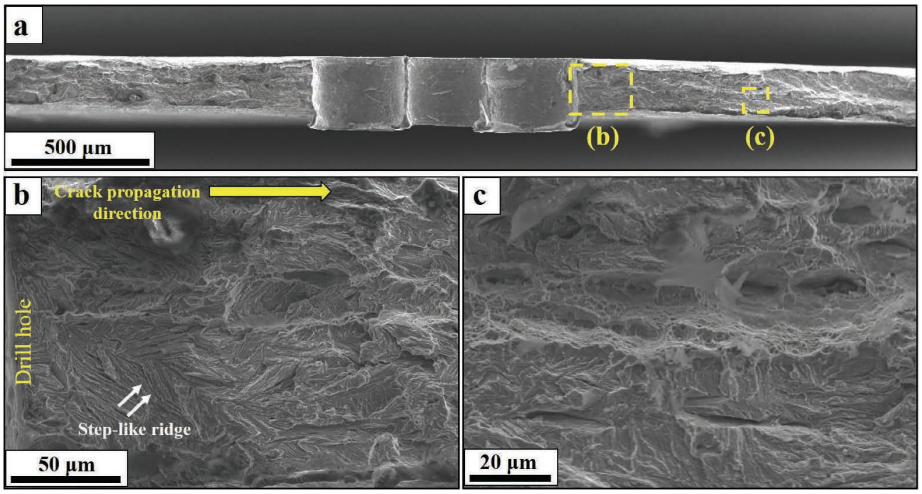

Fig. 14. (a) Overview SEM image of the fracture surface of the hydrogen-charged 3DH specimen. High-magnification details of the areas highlighted in (a) are shown in (b) and (c). (Online version in color.)

3.3. Fractographic Analysis

Figure 12 shows the fracture surface of the 1DH specimen without hydrogen charging. The uncharged specimen exhibits typical ductile fracture surface, which is covered by fine dimples and a few coarse ones (Fig. 12(b)). In addition, the fracture surface shows a certain amount of secondary fracture along the rolling direction, as indicated by arrows in the magnified image in Fig. 12(c). This splitting phenomenon, referred to as delamination, was observed in hydrogen-charged smooth specimens of the same TWIP steel.[22] In the present case, the appearance of delamination is possibly promoted by the presence of stress triaxiality at the micro-drill hole.

Figures 13 and **14** display the fracture surfaces of the hydrogen-charged 1DH and 3DH specimens. The overview and magnified images of the fracture surfaces locally show a quasi-cleavage fracture containing several step-like ridges[30,31] (marked by white arrows in Figs. 13(b) and 14(b)). In addition, higher magnification SEM micrographs (Figs. 13(c) and 14(c)) reveal that a number of dimples are distributed along the quasi-cleavage feature.

4. Discussion

Previous work has demonstrated that in the smooth specimens of the hydrogen-charged bimodal TWIP steel, failure occured due to intergranular crack initiation on the surface of the specimen and in the interior of the specimen, followed by the coalescence of the cracks.[22] As expected, the present experiments demonstrated that the crack initiated from the drill hole, and propagated perpendicular to the tensile direction, as shown in Fig. 4. However, the fractures surfaces did not contain the intergranular features as shown in Figs. 13 and 14.

Considering crack propagation, the growth progressed in a step-by-step manner with increasing displacement. Crack extension occurred within the plastic zone next to the notch and ahead of the advancing crack tip in the hydrogen-charged specimen (Fig. 4), which is one of the primary factors resulting in the step-by-step crack growth with increasing displacement in sufficiently ductile materials.[32,33]

The results shown in Fig. 5 indicate that the cracks experience different stages under displacement controlled monotonic loading until failure: (1) a period without crack growth, (2) a period of crack growth with low rate, and (3)

crack growth with high rate. The effects of hydrogen on crack growth and the effect of the different notch arrangements in the two stages of cracking are explained in the following sections.

4.1. First Stage of Crack Growth

In the early regime of crack growth, referred to as the first stage, the cracks in the hydrogen-charged 3DH specimen grew more rapidly than that in the 1DH specimen with hydrogen charging (0.5 μm/s for 3DH and 0.4 μm/s for 1DH). The dependence of the crack growth rates on initial defect size is reasonable, because the crack with the longer initial defect results in higher stress concentration at the crack tip. The stress accommodation at the crack tip results in large plastic straining, which results in crack initiation in front of the main crack when the plastic strain reaches a critical value for the cracking event. Actually, the crack initiation in front of a crack tip was observed as seen in Fig. 10(a). The cracking events preferentially occurred in the grain interior, regardless of the drill hole arrangements, as shown in Figs. 8(b), 9(b), and 10(b). More specifically, transgranular cracking in TWIP steels has been reported to occur along twin boundaries or result from coalescence of cracks that had formed at twin–twin intersections.[16,22,34] Regarding the crack initiation mechanism, in Fig. 10(b), thick deformation twin plates were observed in the deflection points of the crack (indicated by the white arrows) and at the central part of the small crack (indicated by the yellow arrow). These facts imply that the crack initiation in front of the crack tip is caused by twin-twin or possibly twin-slip interactions. On the other hand, according to Figs. 8(b) and 9(b), the crack propagation paths are not along deformation twin plates. Furthermore, the small crack near the secondary crack shown in Fig. 10(b) is also not aligned along the deformation twin plates. Therefore, the crack coalescence event does not occur along twin boundaries in the present case. The crack growth due to the coalescence of the cracks results in quasi-cleavage features on the fracture surface as shown in Figs. 13 and 14. Furthermore, the presence of step-like ridges and dimples on the fracture surfaces (Figs. 13 and 14) indicate that the quasi-cleavage crack propagated with a discontinuous mechanism. For instance, the formation of step-like ridges has been reported when twin–twin or twin–slip interactions occur.[34,35] Specifically, crack growth with formation of step-like ridges in TWIP steels can occur repeatedly: *i.e.* evolution of a crack tip plastic zone, micro-crack/void formation in front of the main crack tip, and subsequent crack coalescence. In this context, the plastic strain is considered to have four contributions to the crack growth: (1) work hardening, which increases the local stress resulting in twin boundary cracking, (2) the twin density to, which raises the density of crack nucleation sites, (3) defect formation on twin boundaries,[36,37] and (4) hydrogen transport by dislocation motion[38,39] to twin boundaries. The high twin density and highly deformed twin plates can be actually seen in Figs. 7 and 8(b). In addition, a quasi-cleavage fracture surface with step-like ridges, which had been attributed to twin cracking, was observed as shown in Figs. 13(b) and 14(b). These four factors demonstrate the importance of plastic straining induced by stress accommodation at the crack tip and explain the gradual crack propagation to failure in the first stage. The increase in yield strength and in the initial twin density by pre-straining accelerates the transgranular crack growth; thus, it enhances the effect of the drill hole arrangement in the first stage. After this apparently stress/strain-controlled process, the dependence of the crack growth behavior on the initial defect size changed significantly in the second stage, which is discussed in the next section.

4.2. Second Stage of Crack Growth

In contrast to the first stage, crack growth in the 1DH specimen in the second stage was similar to that in the 3DH case. Here, two observations should be noted for the second stage. First, the fractographic features did not change significantly with the increase in the crack length, as shown in Figs. 13(c) and 14(c). Thus, the cracking mechanism did not change for increasing crack length. Second, the apparent stress level in the 1DH case is always significantly higher than that in the 3DH specimens when compared at an identical crack length, c.f. Fig. 6. For instance, the true net sectional stress of the 1DH specimen was approximately 1.5 times higher than that of the 3DH specimen at the total crack length of 1.4 mm. These indicate that unlike in the case of the first stage crack growth, the dependence of the crack growth rate on the initial defect arrangement cannot be explained by considering only the apparent stress level at the crack tip.

To explain the crack growth behavior in the second stage, an additional extrinsic factor needs to be considered. In fact, ductile crack growth has been studied by considering multiple factors that can be classified into two groups: intrinsic and extrinsic factors.[40,41] The intrinsic factors account for the resistance to crack tip deformation, which were already discussed for the first stage. The extrinsic factors represent crack tip shielding mechanisms, which primarily act behind the crack tip to retard crack growth. With increasing crack length, the effects of the extrinsic factors become stronger. The difference between the apparent stress values for identical crack lengths with the same crack growth rate can be explained by considering the intrinsic and extrinsic factors simultaneously. The plastic zones present on crack flanks act behind the crack tip to effectively reduce the driving force for the crack growth. The trace of this effect must appear in the dislocation arrangement in the matrix directly underneath the fracture surface. However, no significant difference in the microstructural features was observed between the hydrogen-charged 1DH and 3DH specimens after failure, c.f. in Fig. 11, because the large amount of pre-strain smeared out any trace of the extrinsic factor. Therefore, in the future, the development of a method based on microstructure characterization is required, to clarify the importance of the extrinsic factor in highly pre-strained materials.

It should also be noted that the factors affecting hydrogen-assisted cracking are not specific features of the bimodal microstructure. The transgranular crack growth path in the first stage occurs in grains that are featured by an internal microstructure such as twins, which has been observed in various solution-treated TWIP steels charged with hydrogen.[4,18,42] The extrinsic factor, which is assumed to

occur in the second stage, depends on the macroscopic mechanical parameters such as yield strength and work hardening rate. Furthermore, hydrogen kinetic effects can also affect both the first and second stages. However, these factors can be analyzed even without resorting to the peculiarities of the bimodal microstructure. Thus, the present results are regarded as demonstrating general features of hydrogen-assisted crack propagation in highly ductile, slightly hydrogen susceptible steels such as TWIP steels.

5. Summary and Conclusions

In the present study, the crack propagation behavior of a pre-deformed TWIP steel under electrochemical hydrogen charging was investigated. The hydrogen-assisted crack growth occurred via a quasi-cleavage process, and the crack growth rate increased upon increasing the effective size of the artificial micro defects when the crack length was small. The stress accommodation at the crack tip resulted in large plastic straining, resulting in work hardening and an increase in twin density. These plasticity-related factors result in a crack formation ahead of the main crack tip. The crack initiation and subsequent coalescence are crack growth processes, and accordingly, the hydrogen-assisted crack growth mechanism is discontinuous, which involves step-like ridges and local formation of dimples on the fracture surface. A strong plastic pre-deformation accelerates the formation of the plasticity-induced precursor of the crack, which is considered to facilitate the transgranular crack propagation mode.

Acknowledgements

This study was financially supported by JSPS KAKENHI (JP16H06365 and JP17H04956).

REFERENCES

1) M. Whiteman and A. Troiano: *Corrosion*, **21** (1965), 53.
2) Y. Oda and H. Noguchi: *Int. J. Fract.*, **132** (2005), 99.
3) M. Martin, S. Weber, W. Theisen, T. Michler and J. Naumann: *Int. J. Hydrog. Energy*, **36** (2011), 15888.
4) M. Koyama, E. Akiyama, K. Tsuzaki and D. Raabe: *Acta Mater.*, **61** (2013), 4607.
5) T. Michler and J. Naumann: *Int. J. Hydrog. Energy*, **35** (2010), 1485.
6) Q. Zhou, L. Qian, J. Tan, J. Meng and F. Zhang: *Mater. Sci. Eng. A*, **578** (2013), 370.
7) M. Koyama, C. C. Tasan, E. Akiyama, K. Tsuzaki and D. Raabe: *Acta Mater.*, **70** (2014), 174.
8) I. B. Tuğluca, M. Koyama, B. Bal, D. Canadinc, E. Akiyama and K. Tsuzaki: *Mater. Sci. Eng. A*, **717** (2018), 78.
9) K. Edalati, T. Furuta, T. Daio, S. Kuramoto and Z. Horita: *Mater. Res. Lett.*, **3** (2015), 197.
10) K. Edalati, S. Toh, T. Furuta, S. Kuramoto, M. Watanabe and Z. Horita: *Scr. Mater.*, **67** (2012), 511.
11) O. Furukimi, C. Kiattisaksri, Y. Takeda, M. Aramaki, S. Oue, S. Munetoh and M. Tanaka: *Mater. Sci. Eng. A*, **701** (2017), 221.
12) J. Yu and J. Kim: *Acta Mater.*, **56** (2008), 5514.
13) S. I. Baik, T. Y. Ahn, W. P. Hong, Y. S. Jung, Y. K. Lee and Y. W. Kim: *Scr. Mater.*, **100** (2015), 32.
14) D. Wan, A. Alvaro, V. Olden and A. Barnoush: *Int. J. Hydrog. Energy*, **44** (2019), 5030.
15) D. Farkas, S. Van Petegem, P. M. Derlet and H. Van Swygenhoven: *Acta Mater.*, **53** (2005), 3115.
16) M. Koyama, E. Akiyama, T. Sawaguchi, D. Raabe and K. Tsuzaki: *Scr. Mater.*, **66** (2012), 459.
17) I. B. Tuğluca, M. Koyama, Y. Shimomura, B. Bal, D. Canadinc, E. Akiyama and K. Tsuzaki: *Metall. Mater. Trans. A*, **50** (2019), 1137.
18) B. Bal, M. Koyama, G. Gerstein, H. Maier and K. Tsuzaki: *Int. J. Hydrog. Energy*, **41** (2016), 15362.
19) Y. Bai, Y. Momotani, M. C. Chen, A. Shibata and N. Tsuji: *Mater. Sci. Eng. A*, **651** (2016), 935.
20) K. G. Chin, C. Y. Kang, S. Y. Shin, S. Hong, S. Lee, H. S. Kim, K. H. Kim and N. J. Kim: *Mater. Sci. Eng. A*, **528** (2011), 2922.
21) R. T. van Tol, L. Zhao, L. Bracke, P. Kömmelt and J. Sietsma: *Metall. Mater. Trans. A*, **44** (2013), 4654.
22) A. Mohammadi, M. Koyama, G. Gerstein, H. J. Maier and H. Noguchi: *Int. J. Hydrog. Energy*, **43** (2018), 2492.
23) I. Gutierrez-Urrutia and D. Raabe: *Scr. Mater.*, **66** (2012), 992.
24) D. Barbier, N. Gey, N. Bozzolo, S. Allain and M. Humbert: *J. Microsc.*, **235** (2009), 67.
25) M. Khedr, L. Wei, M. Na, L. Yu and J. Xuejun: *JOM*, **71** (2019), 1338.
26) Y. Zhong, F. Yin, T. Sakaguchi, K. Nagai and K. Yang: *Acta Mater.*, **55** (2007), 2747.
27) M. Calcagnotto, D. Ponge, E. Demir and D. Raabe: *Mater. Sci. Eng. A*, **527** (2010), 2738.
28) S. S. S. Kumar, T. Raghu, P. P. Bhattacharjee, G. A. Rao and U. Borah: *J. Alloy. Compd.*, **709** (2017), 394.
29) K. S. Suresh, T. Kitashima and Y. Yamabe-Mitarai: *Mater. Sci. Eng. A*, **618** (2014), 335.
30) Y. J. Kwon, J. W. Won, S. H. Park, J. H. Lee, K. R. Lim, Y. S. Na and C. S. Lee: *Mater. Sci. Eng. A*, **732** (2018), 105.
31) G. Park, S. Jeong, H. Kang and C. Lee: *Mater. Charact.*, **139** (2018), 293.
32) K. B. Broberg: *J. Mech. Phys. Solids*, **23** (1975), 215.
33) M. Paredes, T. Wierzbicki and P. Zelenak: *Eng. Fract. Mech.*, **168** (2016), 92.
34) M. Koyama, E. Akiyama, Y. K. Lee, D. Raabe and K. Tsuzaki: *Int. J. Hydrog. Energy*, **42** (2017), 12706.
35) K. A. Nibur, B. P. Somerday, D. K. Balch and C. S. Marchi: *Acta Mater.*, **57** (2009), 3795.
36) S. Mahajan and G. Y. Chin: *Acta Metall.*, **21** (1973), 173.
37) L. Rémy: *Acta Metall.*, **25** (1977), 711.
38) J. Tien, A. W. Thompson, I. M. Bernstein and R. J. Richards: *Metall. Trans. A*, **7** (1976), 821.
39) M. Dadfarnia, M. L. Martin, A. Nagao, P. Sofronis and I. M. Robertson: *J. Mech. Phys. Solids*, **78** (2015), 511.
40) R. O. Ritchie: *Int. J. Fract.*, **100** (1999), 55.
41) M. E. Launey and R. O. Ritchie: *Adv. Mater.*, **21** (2009), 2103.
42) T. Dieudonné, L. Marchetti, M. Wery, J. Chêne, C. Allely, P. Cugy and C. P. Scott: *Corros. Sci.*, **82** (2014), 218.